SCIENTIFIC REPORTS

OPEN

Microscale heat transfer and thermal extinction of a wire-grid polarizer

Received: 27 February 2018
Accepted: 24 September 2018
Published online: 08 October 2018

Seongmin Im[1], Eunji Sim[2] & Donghyun Kim[1]

We explore heat transfer and thermal characteristics of a wire-grid polarizer (WGP) on a microscale by investigating the effect of various geometrical parameters such as wire-grid period, height, and a fill factor. The thermal properties arise from heat transfer by light absorption and conduction in wire-grids. Fill factor was found to be the most dominant geometrical parameter. For TM polarized light, a higher fill factor with thicker wire-grids increased the temperature. The local temperature was found to rise up to $T_{max} = 354.5$ K. TE polarization tended to produce lower temperature. Thermal extinction due to polarimetric extinction by a WGP was also evaluated and highest extinction was observed to be 4.78 dB, which represents a temperature difference $\Delta T = 54.3$ °C. We expect the results to be useful for WGPs in polarization-sensitive thermal switching applications.

A wire-grid polarizer (WGP) is an optical element consisting of wire-grids: TE polarized light with an electric field aligned in an orientation parallel to the wire-grids drives a conduction current and produces Joule heating in the wire (absorption) or re-radiation in the backward direction (reflection)[1]. On the other hand, TM polarized light can propagate through the grids, thereby transmitted or reflected light becomes strongly polarized. A WGP has drawn significant interests, initially as an infrared polarizing element[2], because of the excellent polarization performance combined with planar structure that allows an array-type polarization filter and easy integration to other optical components. For example, a WGP has been integrated to a photodiode[3], liquid crystal[4–7], fiber-optics[8], optical isolators[9,10], semiconductor laser[11], light-emitting diodes[12], contact lens[13], photoelectrochemical solar cells[14], and a CMOS and CCD imaging sensor[15–19]. A WGP has found applications in imaging[20] and spectro-polarimetry[21,22] and also in projection displays[23]. Polarimetry using a biomolecular WGP consisting of hybridizing DNA-nanoparticle composites was reported[24]. In addition, effects of surface roughness were analyzed on WGP performance[25]. A WGP was explored on a rotating platform[26] and flexible surface[27–30], while a plasmonic WGP was investigated based on blazed grating structure[31]. Significant part of WGP research has largely been limited to fabrication issues, such as fabrication of WGPs by way of nanoimprinting[32–37]. Simplified fabrication due to longer wire-grid period requirement allows applications in microwave and terahertz wavebands[30,38,39].

In all these studies, thermal characteristics produced by the energy distribution of light fields have been hardly of interest, as the most attention has been paid to evaluating and optimizing polarimetric performance in the far-field, which is measured by

$$Tr^{TE} = \frac{\langle E_t^{TE} \times H_t^{TE} \rangle}{\langle E_i^{TE} \times H_i^{TE} \rangle} \quad (1)$$

$$Tr^{TM} = \frac{\langle E_t^{TM} \times H_t^{TM} \rangle}{\langle E_i^{TM} \times H_i^{TM} \rangle} \quad (2)$$

$$ER = \left| \frac{\langle E_t^{TM} \times H_t^{TM} \rangle - \langle E_t^{TE} \times H_t^{TE} \rangle}{\langle E_i^{TM} \times H_i^{TM} \rangle + \langle E_i^{TE} \times H_i^{TE} \rangle} \right|. \quad (3)$$

[1]School of Electrical and Electronic Engineering Yonsei University, Seoul, 03722, Korea. [2]Department of Chemistry, Yonsei University, Seoul, 03722, Korea. Correspondence and requests for materials should be addressed to D.K. (email: kimd@yonsei.ac.kr)

Here, *Tr* represents transmittance of TE and TM polarization. *ER* is an extinction ratio of TM over TE polarization. *ER* ranges from 0 (no polarization) to 1 (perfect polarization) and is often defined otherwise as $ER = Tr^{TM}/Tr^{TE}$ with 1 for no polarization and ∞ for perfect polarization. E_i and E_t (H_i and H_t) denote electric (magnetic) field amplitude of incident and transmitted light. $\langle\ \rangle$ refers to a time and space average of light fields in the far-field. Inside the bracket is, in fact, the Poynting vector of a light field. As WGP structure finds increasingly more applications on a micro and nanoscale, thermal characteristics become extremely important to understand, because light energy can give rise to thermal fluctuations and, thereby, affect the performance of devices that are integrated to a WGP. For this reason, thermal properties have drawn significant interests in nanoscale optical devices, such as metal and dielectric nanorods[40,41] and plasmonic nanospheres[42]. Many studies have been performed to understand thermal radiation in a nanoscale gap[43,44]. Near-field heat transfer was investigated between gratings[45]. Thermal properties of magnetic nanoparticles were simulated for hyperthermia treatment of cancer[46], while thermal resistance was measured and estimated for tungsten silicide WGPs to be high up to 523 K[47].

In this paper, we intend to compute and analyze thermal distributions produced by a WGP. The thermal distribution can be far from replicating the distribution of light fields because of finite thermal conductivity and radiation in the microscale range. For applications as a polarizing element in an optical set-up and particularly when a WGP is integrated as a part of a device or a package, e.g., grating wire-grids used as a biosensing substrate on which molecular interactions may be measured[48–51], the thermal distribution on a WGP may affect the biosensor performance and, therefore, exact understanding of thermal characteristics of a WGP is vital. Furthermore, as we explore thermal extinction between the two polarization components, understanding the thermal characteristics may go beyond WGPs and can be a basis for opening novel applications. Polarization-dependent thermal stimulus may be used to develop a new tool for cell-based assays in biomedical applications using thermal "hot" spots to turn on or off molecular processes or an electronic device that can be thermally switched to control and modulate heat transfer electronically with improved functional characteristics.

Numerical Method and Model

Calculation of wave-coupled heat transfer equation. For calculation of thermo-optic characteristics produced by WGP structures, wave-coupled time-dependent heat transfer equation was solved, which is given as follows[52–54]:

$$C_s\rho\frac{\partial T}{\partial t} + \mathbf{n}\cdot\boldsymbol{q} = \frac{1}{2}\varepsilon_0\omega Im(\varepsilon_r)|E|^2 \tag{4}$$

$$-\mathbf{n}\cdot\boldsymbol{q} = \nabla\cdot[k\nabla T + h(T_{amb} - T) + \varepsilon_m\sigma(T_{amb}^4 - T^4)] \tag{5}$$

$$\nabla^2 E - \mu\varepsilon\frac{\partial^2 E}{\partial t^2} = 0 \tag{6}$$

Eq. (4) is the heat transfer equation with the right-hand side referring to the dissipated heat that is generated by electromagnetic absorption and acts as a heat source. **n** and $\boldsymbol{q}$ are the normal vector to the lateral plane and heat. The three terms in the del operator on the right-hand side of Eq. (5) represent the heat transfer by conduction, convection, and radiation, respectively. Eq. (6) is the wave equation that describes wave propagation in a medium with ε and μ as the medium permittivity and permeability. C_s represents the heat capacity, while ρ is the medium density and k thermal conductivity. ω is the angular frequency of incident light. h is the convective heat transfer coefficient and T_{amb} the ambient temperature. ε_m denotes the emissivity of metal (gold in our case) and σ the Stefan–Boltzmann constant. $E(\mathbf{r}, t)$ and $T(\mathbf{r}, t)$ denote the spatial distribution of electric field amplitude and temperature. The wave equation in Eq. (6) was solved by frequency analysis using time-independent method and the heat transfer equation of Eq. (4) by time-dependent analysis. Electromagnetic waves were assumed to have a constant field distribution while heat was spreading, because electromagnetic wave propagation is much faster than heat transfer by conduction. This assumption in thermo-optic calculations leads to quasi-static solutions that are in effect much simpler to attain than fully time-dependent approaches.

Note that the difference of the incident power from what is dissipated by WGP may cause imperfect matching between optical calculation and that of heat transfer equation. Furthermore, it is difficult to apply boundary conditions to semi-infinite structures, such as grating, particularly in the case of heat transfer equation, because modeling the heat transferred between cells is tricky when a heat source is in contact with the boundary. These issues were addressed by performing aperiodic calculation on WGP structures, instead of considering wave and heat transfer equation separately over the entire structure which may require heavy memory consumption[55,56].

Numerical methods. Far-field characteristics of a WGP were calculated with rigorous-coupled wave analysis (RCWA) using 40 spatial harmonics. For wave optics calculation of optical characteristics, 2D finite element method (FEM) on COMSOL™ was used under scattering and periodic boundary condition with triangular meshes of 0.045 to 22.5 nm in size. Periodic calculation using 2D FEM in the far-field was confirmed with RCWA and 3D FEM models and found to be in agreement.

Thermal properties of WGPs were also calculated using FEM which implemented Eqs (4 and 5). FEM calculation was performed with an incident light intensity at 0.1 mW/μm² under scattering boundary conditions. The intensity was taken as a value that may be obtained under typical experimental conditions. Calculation was also performed with 0.01 mW/μm² as incident intensity for comparison. For the calculation of heat transfer equation, we used a heat flux boundary condition with a heat transfer coefficient set at $h = 5$ W/K·m², which is taken from literature[54], and an external ambient temperature at $T_{amb} = 293.15$ K (room temperature). The substrate

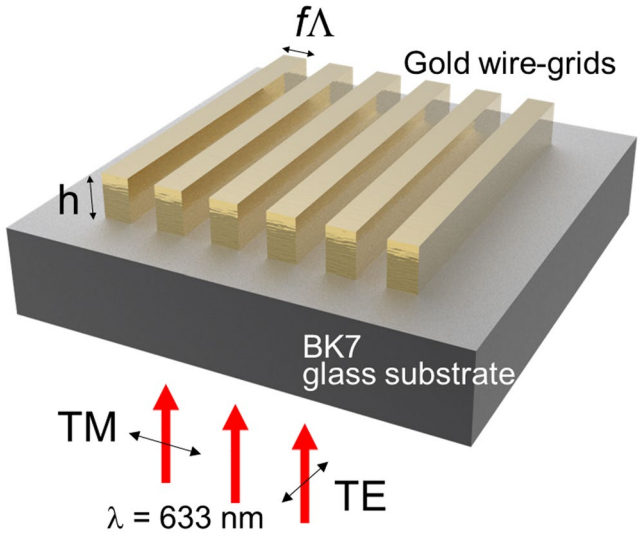

Figure 1. Schematic illustration of a WGP numerical model with wire-grid period Λ, fill factor f, and height h. The direction of electric field oscillation for TM and TE polarized light is also shown.

was assumed to form periodic boundaries in the lateral direction with a heat transfer coefficient at 0 W/K·m^2 and grating wires as an electromagnetic heat source. The steady-state temperature was measured at the center of wire-grid surface.

Numerical model for WGP. The schematic of the numerical model employed for computation is presented in Fig. 1. Wire-grid of gold in a rectangular surface profile is assumed on a BK7 glass substrate in air ambiance. Wire-grid periods for numerical computation were varied in a range of $\Lambda = 500$ nm~1 μm in a step of 100 nm (for RCWA calculation, $\Lambda = 400$ nm~1 μm with a 10-nm step). The wire-gird thickness or grid height (h) and fill factor (f) were varied to be $h = 100$~500 nm and $f = 0.1$~0.9. It was assumed that monochromatic plane waves of linear polarization were of normal incidence at $\lambda = 633$ nm. Polarization direction corresponding to TM/TE polarized light is also shown in Fig. 1. Throughout computation, refractive index of BK7 glass substrate was set to be $n_s = 1.5151$. For the simplicity of calculation, the substrate was assumed to be thick by 5Λ from 2.5 to 5 μm, an assumption often used in related studies[41,53]. For gold, refractive index was interpolated from reference[57]. We have also assumed that only the zeroth order reflection or transmission is collected by detectors.

Metrics of WGP performance. As mentioned earlier, the performance of a WGP was assessed with transmittance (Tr) and extinction ratio (ER). ER was represented as $ER = 10\log(Tr^{TM}/Tr^{TE})$ in dB. Similarly, we have evaluated thermal characteristics of a WGP with temperature, T^{TM} and T^{TE} (in Kelvin), measured at the center of WGP surface for both polarization components, and also thermal extinction ratio ($ThER$), which we define as the ratio of average local temperature in Celsius for TM to that of TE, i.e.,

$$ThER = \frac{T^{TM}}{T^{TE}} \quad \text{or} \quad 10\log\left(\frac{T^{TM}}{T^{TE}}\right) \text{ in dB} \tag{7}$$

$ThER$ reflects on the extinction based on point measurements at the surface. $ThER$ should be interpreted simply as a ratio of temperature in Celsius induced with TM polarized light over TE polarization, rather than as a measure of power or heat.

Results and Discussion

Far-field optical properties of a WGP. Far-field characteristics of a WGP, while well-known, were calculated for confirmation of results, as shown in Fig. 2. Grating equation at normal incidence is given by $k\sin\theta_m = mK_G/n_s$ for substrate modes and $k\sin\theta_m = mK_G$ for ambient modes, where $k = 2\pi/\lambda$ and $K_G = 2\pi/\Lambda$ represent the incident wave number and the magnitude of grating vector. m is an integer used for diffraction orders. θ_m denotes the angle of outgoing waves after diffraction. Grating equation shows that Rayleigh anomaly occurs as a result of energy redistribution between diffraction orders for WGP with $\Lambda > \Lambda_{s1}^{RA} = \lambda/n_s = 418$ nm. In the range of wire-grid periods that we calculate in this work, the energy redistribution takes place at $\Lambda = 418$ (Λ_{s1}^{RA}), 633 (Λ_{a1}^{RA}), and 836 nm (Λ_{s2}^{RA}). Figure 2 shows transmittance (Tr) and extinction (ER) produced by a WGP at $h = 100$ and 200 nm. A clear trend presented in Fig. 2 is that transmittance overall decreases, while ER increases, with a higher fill factor f, i.e., incident light is largely transmitted (reflected) at a low (high) f due to the smaller (larger) volume of absorbing metal. For thick WGPs with height on the order of several hundred nanometers, metal-dielectric-metal waveguide modes in the vertical direction may also induce resonances and high absorption with TM polarized light incidence, although the resonance may be weakened at small periods[58]. Maximum ER attained with $h = 200$ nm was 2280, although in this case transmittance was low at 6.25%. Similar to the effect of a fill factor, thicker wire-grids tend to increase extinction, while decreasing transmittance.

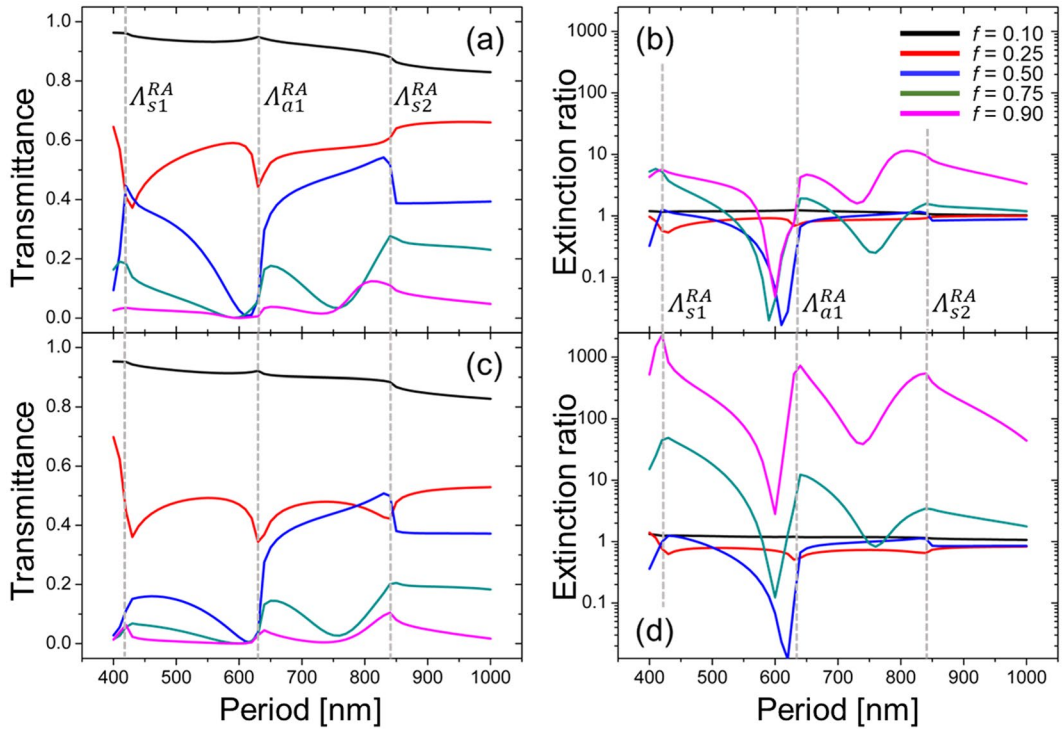

Figure 2. (**a**) Transmittance and (**b**) *ER* of a WGP at normal incidence for $\Lambda = 400\sim1000$ nm with wire-grid height $h = 100$ nm. (**c**) Transmittance and (**d**) *ER* for $h = 200$ nm. The fill factor f is varied. Λ_{sm}^{RA} and Λ_{am}^{RA} represent the grating period at which Rayleigh anomaly occurs due to m-th substrate and ambient modes (marked in gray dotted lines).

Thermal properties of a WGP. Figure 3 presents the equilibrium temperature calculated at the center of a WGP for TE and TM polarized light. The temperature induced by TM polarization is overall significantly higher than for TE polarized light with a maximum as high as T = 354.5 K when $\Lambda = 600$ nm, $f = 0.75$, and $h = 200$ nm. For comparison, maximum temperature reached by TE polarized light is T = 334.6 K when $\Lambda = 1\,\mu$m, $f = 0.75$, and $h = 500$ nm. The parameters with which the highest temperature is produced are marked by arrows in Fig. 3. The distinct temperature characteristics between polarization components of a WGP is associated with the physical origin of heat transfer induced by TE and TM polarized light. For TE polarization, conductive heat transfer by way of Joule heating that is produced by significant light absorption is dominant. In the case of TM polarization, radiative heat transfer by plasmon-polaron resonant modes dominates, where polaron mode is coupled to plasmon states created by momentum-matching with incident photon in metallic wire-grids. While polaron-plasmon coupling in split-ring resonator (SRR) structure was reported previously[59], WGPs are presumed to make a more significant temperature difference between TE and TM polarization components than SRRs due to the inherent polarimetric extinction. Heat spreading takes place through ambient air and glass substrate largely by conduction and radiative wave propagation and, to a lesser extent, excitation of surface plasmon polariton modes on the wire-grid/glass substrate interface[60,61]. Thermal fluctuating currents may produce net emission, although its mean is zero. The effect compared to the ambience is estimated to be minor in terms of autocorrelation, according to the fluctuation-dissipation theorem[62].

Trivariate linear regression analysis was performed with period, height, and fill factor of wire-grids as independent variables. Table 1 shows that a linear model fits better to TM polarization with higher correlation over TE polarization, although it may well be a weak predictor of parameter-dependence of temperature, and suggests the fill factor to be the strongest parameter that affects temperature. For TE polarized light, the effect of wire-grid height is almost as important as that of fill factor. Temperature is positively correlated with a fill factor f, presumably because of heat flux associated with absorption cross-section of metallic wire-grids and due to the excitation of guided modes and surface plasmon when the corrugation depth is increased[63]. This encourages more light absorption and more active heat transfer by thermal conduction at the grid-air interface. For TM polarization, although a large part of energy is transmitted, there is still significant absorption which gives rise to heat transfer by conduction and therefore higher $\partial T/\partial f$. In contrast, TE polarized light is largely reflected, rather than absorbed, so that the volume effect represented by the fill factor manifests itself weakly. As a result, $\partial T/\partial f$ is lower with weaker correlation between the temperature and the fill factor. In fact, the time derivative $\partial T/\partial f$ is 2.60 (=1090/420) times higher for TM polarized light than TE, indicating that an increase of fill factor leads to a higher temperature rise in the case of TM polarization.

The temperature distribution of a WGP with geometric parameters which produce the highest local temperature is shown in Fig. 4. TM-polarized light forms higher temperature distribution along the depth (z) axis and transmissive electric fields through metal wire-grids. Due to more active heat transfer, thermal energy of TM

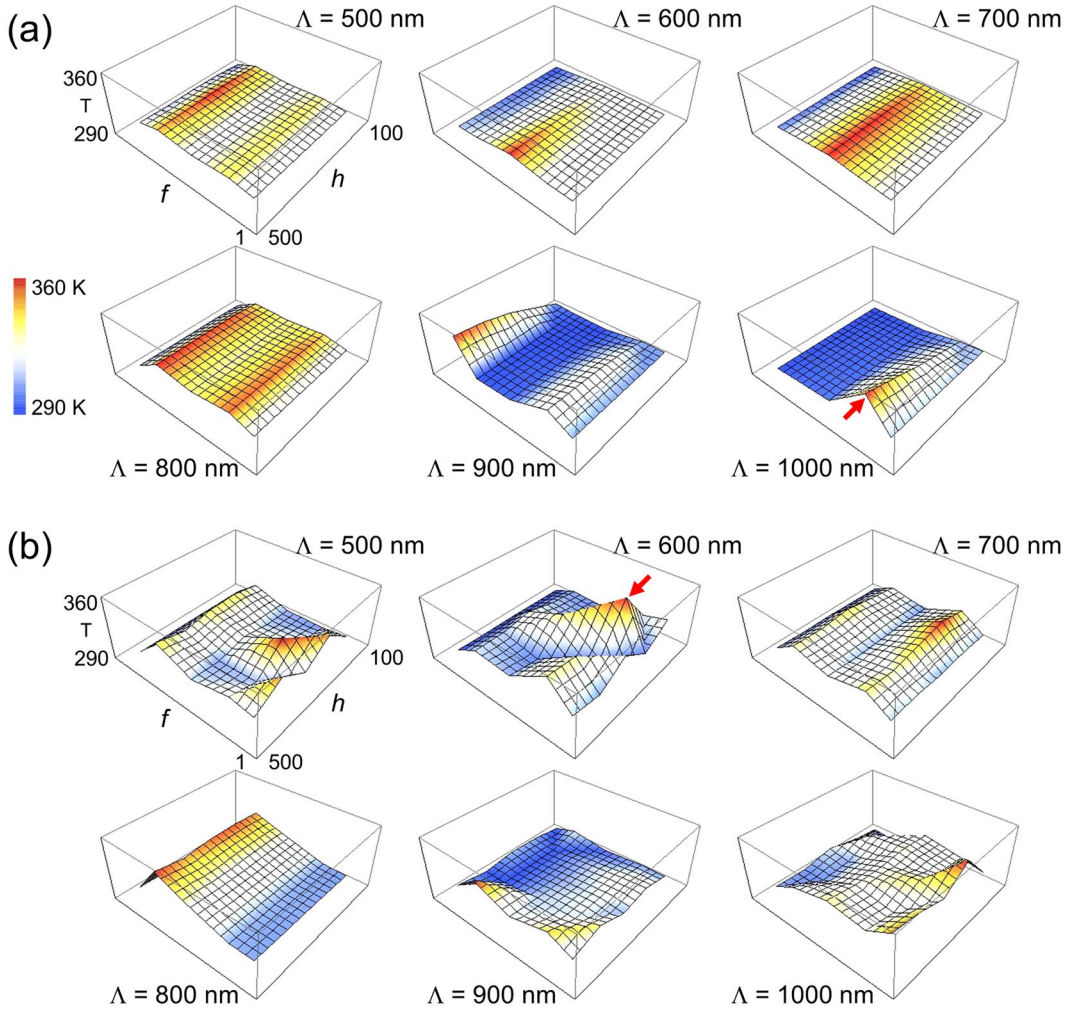

Figure 3. Temperature distribution produced by a WGP for wire period $\Lambda = 500\,\text{nm}\sim1\,\mu\text{m}$, fill factor $f = 0.1\sim0.9$, and grating height $h = 100\sim500\,\text{nm}$: (**a**) TE and (**b**) TM polarization. Temperature in absolute temperature (K). Red arrows represent the parameters that produce maximum temperature for TE and TM polarized light: $T_{max} = 334.6\,\text{K}$ at $\Lambda = 1\,\mu\text{m}$ and $h = 500\,\text{nm}$ (TE) vs. 354.5 K at $\Lambda = 600\,\text{nm}$ and $h = 200\,\text{nm}$ (TM). For both cases, $f = 0.75$.

	TE polarization		TM polarization	
	Temperature derivative	P-R^2	Temperature derivative	P-R^2
$\partial T/\partial \Lambda$ [K/μm]	4.25 ± 3.37	0.101	6.69 ± 5.03	0.104
$\partial T/\partial h$ [K/μm]	8.54 ± 4.07	0.168	9.91 ± 6.07	0.127
$\partial T/\partial f$ [K/%]	0.0420 ± 0.0193	0.174	0.1090 ± 0.0288	0.296
R^2	0.0685		0.115	

Table 1. Temperature derivatives with respect to the geometrical parameters for TE and TM polarization as a result of trivariate linear regression analysis (s.d. n = 150, P-R^2: Pearson correlation coefficient, and R^2: coefficient of multiple determination).

polarization dissipates slightly faster in the depth axis at a rate of $\Delta T/\Delta z = -73.7\,\text{K/mm}$ than that of TE polarization ($\Delta T/\Delta z = -49.6\,\text{K/mm}$). In general, temperature changes very slowly along the depth axis on the order that is in line with literature[64,65]. It is also interesting that TM polarization induces much less prominent lateral (x) heat flux component than TE polarization.

Different perspectives can be obtained in Fig. 5, which presents equilibrium temperature in terms of grating height *h* and a fill factor *f*. Clearly, the effect of fill factor appears to prevail in the temperature characteristics while that of grating height is weak. On the other hand, the effect of wire-grid period is relatively inconspicuous in line with what we observed in Fig. 3 and Table 1. Temperature variation is also significantly higher with TM polarized light. For TE polarization, much part of light is absorbed and reflected by wire-grids regardless of the period,

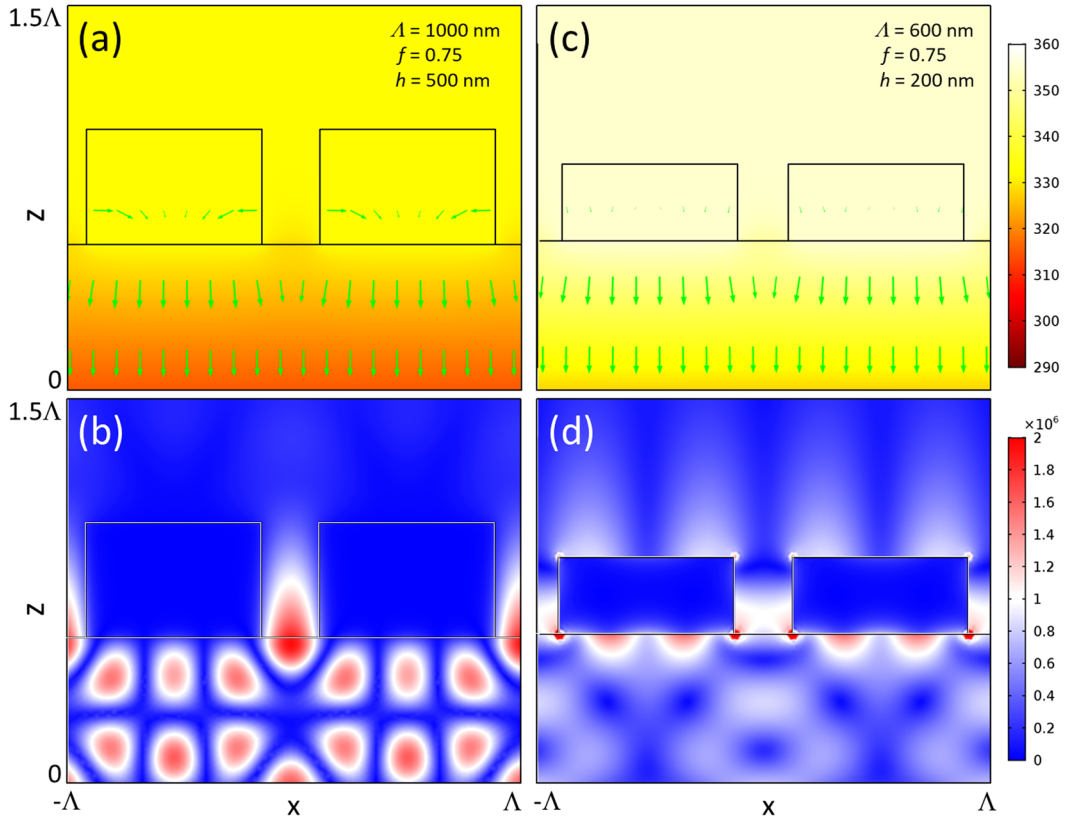

Figure 4. (**a**) Spatial distribution of local temperature and (**b**) electric field amplitude ($|E^{TE}|$) produced by a WGP: $\Lambda = 1000$ nm, $f = 0.75$, and $h = 500$ nm with normal light incidence along +z direction in TE polarization (Max: 331.76 K and Min: 331.71 K). (**c**) Temperature and (**d**) electric field ($|E^{TM}|$): $\Lambda = 600$ nm, $f = 0.75$, and $h = 200$ nm with TM polarized light (Max: 354.59 K and Min: 354.56 K). Arrows represent the direction and strength of heat flux. Data at 5 μs after light illumination. Temperature in unit of K and electric field in V/m.

therefore the temperature varies with even weaker dependence on wire-grid period. Somewhat erratic behavior of temperature characteristics in the case of TM polarization is presumed to be associated with Rayleigh anomaly. In contrast, a significant portion of TE polarized light is extinguished by metal wires, therefore the effect of Rayleigh anomaly is less severe.

In short, fill factor was found to be the most dominant parameter that affects the temperature. The dependence is stronger in TM polarization than for TE polarized light. Dependence on the wire-grid height and period is weaker over the range that we calculated. TM polarization induces higher variation in the observed temperature with respect to the period.

Aside from the effects of various geometrical parameters, it is worth a note that the near-fields produced by a WGP in air ambience may induce local temperature almost as high as 355 K with an incident light intensity at 0.1 mW/μm^2. Although not with WGPs, such a high temperature induced in the micro and nanoscale range was observed experimentally, for example, in plasmonic heating[66–68]. Note that heat transfer depends heavily on environmental effects of ambience. Preliminary calculations in water ambience show that the maximum temperature in the steady-state remains lower than in air, because of higher heat capacity of water than that of air (roughly 4.18 vs. 1.00 J). Also, thermal conductivity for water is much higher than air, for example, by more than 20 times under atmospheric pressure and room temperature (0.6096 W/K·m for water vs. 0.02623 W/K·m for air)[69,70], therefore relaxation of heat takes place on a faster scale.

Microscale thermal extinction. We now investigate thermal extinction *ThER* achieved by a WGP. Figure 6 shows *ThER* as a function of a fill factor f and wire-grid height h for wire-grid period Λ. The thermal extinction can be important for example, in applications where a polarization-dependent temperature change may induce a process on or off. Gray areas in Fig. 6 represent a region with $ThER < 1$, i.e., the temperature produced by TM polarized light becomes lower than that of TE polarization. Highest extinction was observed as $ThER_{max} = 3.00$ (or 4.78 dB) when $\Lambda = 600$ nm, $f = 0.75$, and $h = 200$ nm. While the maximum thermal extinction ratio may not appear to be significant, the value represents a remarkable temperature difference $\Delta T = 54.3$ K, which can be switched on or off by the transition of polarization states. If we consider imaging applications, for example, imaging polarimetry, typical optical input scenes to a WGP consist of mixed polarization components and the results in Fig. 6 suggest that local temperature may vary significantly depending on the input polarization content. On the other hand, this also implies that local temperature may be adjusted with precision by controlling the incident light polarization. Interestingly comparison of Figs 3 and 6 shows that the WGP structure corresponding to the

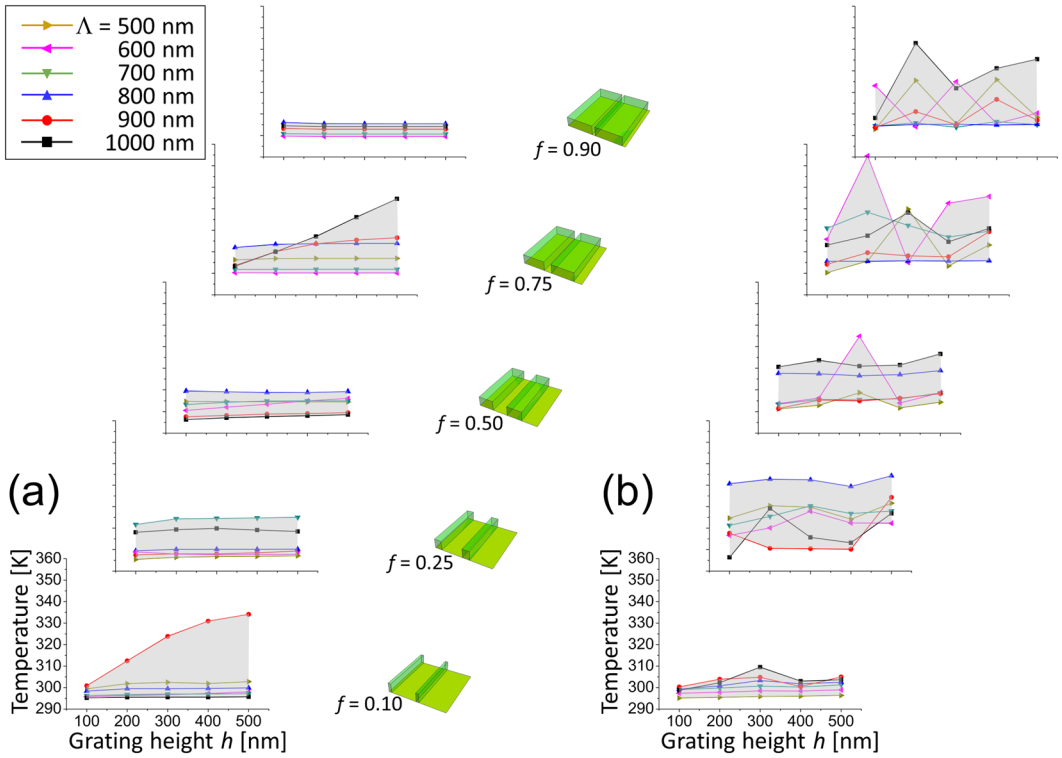

Figure 5. Temperature characteristics produced by a WGP with a fill factor $f = 0.1{\sim}0.9$, and grating height $h = 100{\sim}500$ nm: (**a**) TE and (**b**) TM polarization. Shaded area represents the temperature variation with respect to wire-grid periods. WGP schematics corresponding to each fill factor are also shown.

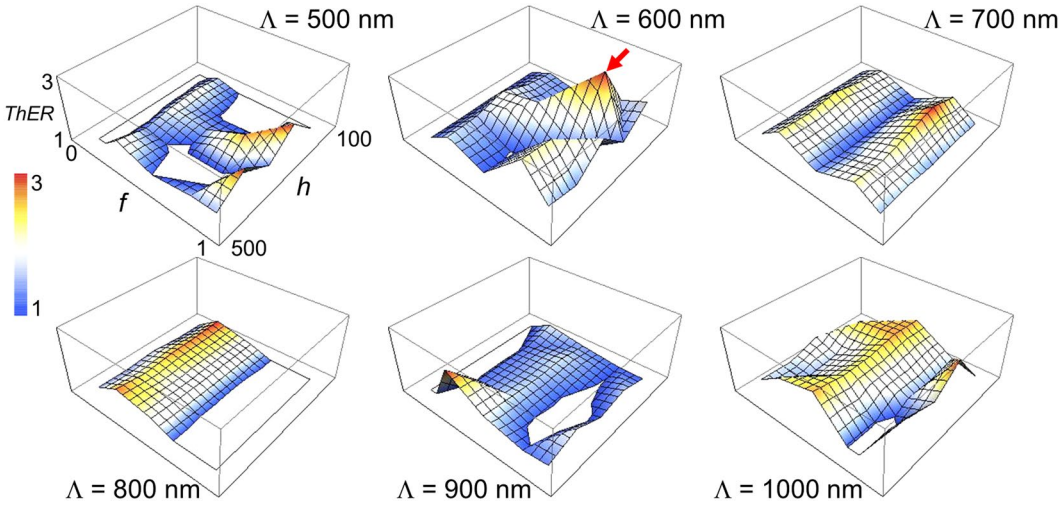

Figure 6. Thermal extinction ratio (*ThER*) of a WGP with a fill factor $f = 0.1{\sim}0.9$, and grating height $h = 100{\sim}500$ nm for wire-grid period $\Lambda = 500$ nm~1 μm. Gray represents an area of $ThER < 1$. Highest $ThER = 3.00$ observed at $f = 0.75$ and $h = 200$ nm with $\Lambda = 600$ nm (marked by arrow).

highest optical and thermal extinction is almost identical, suggesting that optical extinction provided by primarily transmissive TM light component gives rise to the thermal extinction.

Non-equilibrium dynamics. So far, we have investigated steady-state thermal characteristics of a WGP assuming that heat is dissipated fast enough to reach a steady-state. We now explore thermal relaxation time (τ) that takes for a WGP to reach an equilibrium in the stead-state. The relaxation time was extracted from an exponential fit of temperature-time responses and calculation was performed up to 20 μs to ensure that the steady-state is reached. Within the relaxation time, temperature characteristics may vary significantly from the steady-state. Although the way that the temperature rises presented in the temperature-time response of Fig. 7(a,b) may look

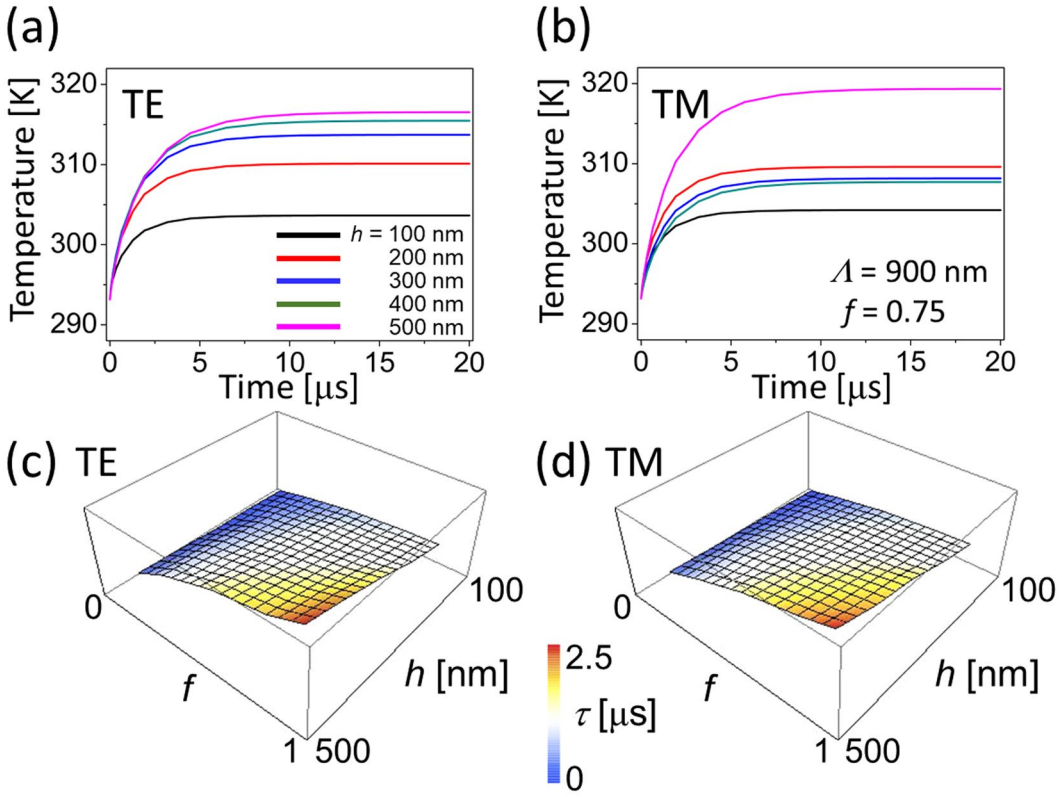

Figure 7. Temperature-time response for a WGP with a period $\Lambda = 900$ nm (wire-grid height h is varied): (**a**) TE and (**b**) TM polarization at $f = 0.75$. Relaxation time (τ) in a 3D plot as a fill factor and a wire-grid height are varied: (**c**) TE and (**d**) TM polarization. Calculation performed up to 20 μs to ensure steady-state.

Input power [mW/μm²]		$T_{max}/T_{min}/\Delta T$ [K]	WGP structure		
			Λ [nm]	f	h [nm]
0.01	TE	297.3/293.4/3.9	1000	0.75	500
	TM	299.3/293.3/6.0	600		200
0.1	TE	334.6/295.2/39.4	1000		500
	TM	354.5/295.1/59.4	600		200

Table 2. Temperature characteristics with an incident light intensity at 0.01 and 0.1 mW/μm² (T_{max} and T_{min}: highest and lowest temperature, $\Delta T = T_{max} - T_{min}$).

different between TE and TM polarization, the relaxation time is surprisingly similar as shown in Fig. 7(c,d). The ratio of relaxation times (τ_{TM}/τ_{TE}) ranged from 0.857~1.450, i.e., the ratio of relaxation times was found to be largely uniform within 15% and much lower than optical or thermal extinction, because the thermal process by which the steady-state is reached through absorption and conduction is in principle identical for both TE and TM polarization. Overall, the relaxation time was on the order of μs (10^{-6} sec), which agrees well with experimental results observed in comparable structures[52]. The relaxation time varies depending on geometrical parameters. First, thicker wire-grids would make thermal energy transfer difficult and therefore relaxation time longer. On the other hand, while a longer wire-grid period increases the relaxation time, the dependence on the fill factor was relatively weak.

Effect of light intensity. While all of the above temperature characteristics of a WGP were obtained with 0.1 mW/μm², we have also explored 0.01 mW/μm² as light intensity to investigate the effect of incident power. The highest temperature was calculated to be 299.3 K for TM and 297.3 K for TE polarization, as listed in Table 2. It is suggested that the induced temperature distribution may be in the linear regime in the sense that the temperature rise due to light incidence, which is represented by ΔT ($=T_{max} - T_{min}$), is linearly related to the input intensity. With much higher intensity beyond the order of 10 mW/μm², the temperature increase was found to become sub-linear likely due to the effects of nonlinear optics, although more exhaustive investigation is needed to understand the specific nature of the power dependence.

Concluding Remarks

As a summary, we have investigated microscale thermo-optic properties of a WGP. It was found that local temperature may rise up to almost 355 K over 80 °C under the given parameters with an incident power at 0.1 mW/μm^2. Although the dependence was not strong enough to generalize for an arbitrary WGP structure, TM polarization overall induces higher temperature than TE polarized light, with increased temperature at higher fill factor. In the parameter space that we have considered, a WGP offers significant thermal extinction by 3 times (or 4.78 dB) in terms of *ThER* for $\Lambda = 600$ nm, $f = 0.75$, and $h = 200$ nm, which represents more than 54 °C in temperature difference by polarization switching between TE and TM. We have also explored relaxation dynamics in a WGP. The results may be useful for understanding thermal characteristics of a WGP and providing thermal extinction for applications that may require polarization-dependent switching of heat transfer.

References

1. Hecht, E. *Optics* (Pearson, 2016).
2. Bird, G. R. & Parrish, M. The wire grid as a near-infrared polarizer. *J. Opt. Soc. Am.* **50**, 886–891 (1960).
3. Doumuki, T. & Tamada, H. An aluminum-wire grid polarizer fabricated on a gallium–arsenide photodiode. *Appl. Phys. Lett.* **71**, 686–688 (1997).
4. Xu, M., Urbach, H., De Boer, D. & Cornelissen, H. Wire-grid diffraction gratings used as polarizing beam splitter for visible light and applied in liquid crystal on silicon. *Opt. Express* **13**, 2303–2320 (2005).
5. Kim, S. H. *et al.* Fabrication of a nano-wire grid polarizer for brightness enhancement in liquid crystal display. *Nanotechnology* **17**, 4436, https://doi.org/10.1088/0957-4484/17/17/025 (2006).
6. Ge, Z. *et al.* Single cell gap and wide-view transflective liquid crystal display using fringe field switching and embedded wire grid polarizer. *Appl. Phys. Lett.* **92**, 051109, https://doi.org/10.1063/1.2841847 (2008).
7. Seo, J. S., Yeom, T. E. & Ko, J. H. Experimental and simulation study of the optical performances of a wide grid polarizer as a luminance enhancement film for LCD backlight applications. *J. Opt. Soc. Korea* **16**, 151–156 (2012).
8. Feng, J. *et al.* A transflective nano-wire grid polarizer based fiber-optic sensor. *Sensors* **11**, 2488–2495 (2011).
9. Wang, J. J. *et al.* Innovative high-performance nanowire-grid polarizers and integrated isolators. *IEEE J. Sel. Topics Quantum Electron.* **11**, 241–253 (2005).
10. Wang, J. J. *et al.* Monolithically integrated isolators based on nanowire-grid polarizers. *IEEE Photon. Technol. Lett.* **17**, 396–398 (2005).
11. Yu, N. *et al.* Semiconductor lasers with integrated plasmonic polarizers. *Appl. Phys. Lett.* **94**, 151101, https://doi.org/10.1063/1.3093476 (2009).
12. Sepsi, Ö., Szanda, I. & Koppa, P. Investigation of polarized light emitting diodes with integrated wire grid polarizer. *Opt. Express* **18**, 14547–14552 (2010).
13. Hollowell, A. E. & Guo, L. J. Nanowire grid polarizers integrated into flexible, gas permeable, biocompatible materials and contact lenses. *Adv. Opt. Mater.* **1**, 343–348 (2013).
14. Nemes, C. T., Koenigsmann, C. & Schmuttenmaer, C. A. Functioning Photoelectrochemical Devices Studied with Time-Resolved Terahertz Spectroscopy. *J. Phys. Chem. Lett.* **6**, 3257–3262 (2015).
15. Tokuda, T., Yamada, H., Sasagawa, K. & Ohta, J. Polarization-analyzing CMOS image sensor using monolithically embedded polarizer for microchemistry systems. *IEEE International Symposium on Circuits and Systems* **2009**, 313–316 (2009).
16. Gruev, V., Perkins, R. & York, T. CCD polarization imaging sensor with aluminum nanowire optical filters. *Opt. Express* **18**, 19087–19094 (2010).
17. Sarkar, M., Bello, D. S. S., van Hoof, C. & Theuwissen, A. Integrated polarization analyzing CMOS image sensor for material classification. *IEEE Sensors J.* **11**, 1692–1703 (2011).
18. Wu, X., Zhang, M., Engheta, N. & van der Spiegel, J. Design of a monolithic CMOS image sensor integrated focal plane wire-grid polarizer filter mosaic. *IEEE Custom Integrated Circuits Conference* **2012**, 1–4 (2012).
19. Sasagawa, K. *et al.* Image sensor pixel with on-chip high extinction ratio polarizer based on 65-nm standard CMOS technology. *Opt. Express* **21**, 11132–11140 (2013).
20. Kim, D. Performance uniformity analysis of a wire-grid polarizer in imaging polarimetry. *Appl. Opt.* **44**, 5398–5402 (2005).
21. Kim, D., Warde, C., Vaccaro, K. & Woods, C. Imaging multispectral polarimetric sensor: single-pixel design and fabrication. *Appl. Opt.* **42**, 3756–3764 (2003).
22. Kim, D. & Burke, K. Design of a grating-based thin film filter for broadband spectro-polarimetry. *Appl. Opt.* **42**, 6321–6326 (2003).
23. Yu, X. J. & Kwok, H. S. Application of wire-grid polarizers to projection displays. *Appl. Opt.* **42**, 6335–6341 (2003).
24. Yu, H., Oh, Y., Kim, S., Song, S. H. & Kim, D. Polarization extinction-based detection of DNA hybridization *in situ* using a nanoparticle wire-grid polarizer. *Opt. Lett.* **37**, 3867–3869 (2012).
25. Ryu, H., Yoon, S. J. & Kim, D. Influence of surface roughness on the polarimetric characteristics of a wire-grid polarizer. *Appl. Opt.* **47**, 5715–5721 (2008).
26. Kim, D. Polarization characteristics of a wire-grid polarizer in a rotating platform. *Appl. Opt.* **44**, 1366–1371 (2005).
27. Kim, D. & Sim, E. Segmented coupled-wave analysis of a curved wire-grid polarizer. *J. Opt. Soc. Am. A* **25**, 558–565 (2008).
28. Meng, F. *et al.* Fabrication and characterization of bilayer metal wire-grid polarizer using nanoimprint lithography on flexible plastic substrate. *Microelectron. Eng.* **88**, 3108–3112 (2011).
29. Shin, Y. J. *et al.* Facile route of flexible wire grid polarizer fabrication by angled-evaporations of aluminum on two sidewalls of an imprinted nanograting. *Nanotechnology* **23**, 344018, https://doi.org/10.1088/0957-4484/23/34/344018 (2012).
30. Ferraro, A. *et al.* Flexible terahertz wire grid polarizer with high extinction ratio and low loss. *Opt. Lett.* **41**, 2009–2012 (2016).
31. Lee, C., Sim, E. & Kim, D. Blazed wire-grid polarizer for plasmon-enhanced polarization extinction: design and analysis. *Opt. Express* **25**, 8098–8107 (2017).
32. Tamada, H., Doumuki, T., Yamaguchi, T. & Matsumoto, S. Al wire-grid polarizer using the s-polarization resonance effect at the 0.8-μm-wavelength band. *Opt. Lett.* **22**, 419–421 (1997).
33. Yu, X. J. & Kwok, H. S. Optical wire-grid polarizers at oblique angles of incidence. *J. Appl. Phys.* **93**, 4407–4412 (2003).
34. Ahn, S. W. *et al.* Fabrication of a 50 nm half-pitch wire grid polarizer using nanoimprint lithography. *Nanotechnology* **16**, 1874, https://doi.org/10.1088/0957-4484/16/9/076 (2005).
35. Wang, J. J. *et al.* 30-nm-wide aluminum nanowire grid for ultrahigh contrast and transmittance polarizers made by UV-nanoimprint lithography. *Appl. Phys. Lett.* **89**, 141105, https://doi.org/10.1063/1.2358813 (2006).
36. Ahn, S. H., Kim, J. S. & Guo, L. J. Bilayer metal wire-grid polarizer fabricated by roll-to-roll nanoimprint lithography on flexible plastic substrate. *J. Vacuum Sci. Technol. B* **25**, 2388–2391 (2007).
37. Schlachter, F. *et al.* UV-NIL based nanostructuring of aluminum using a novel organic imprint resist demonstrated for 100 nm half-pitch wire grid polarizer. *Microelectron. Eng.* **155**, 118–121 (2016).
38. Yamada, I., Takano, K., Hangyo, M., Saito, M. & Watanabe, W. Terahertz wire-grid polarizers with micrometer-pitch Al gratings. *Opt. Lett.* **34**, 274–276 (2009).

39. Cetnar, J. S. *et al*. Extraordinary optical transmission and extinction in a Terahertz wire-grid polarizer. *Appl. Phys. Lett.* **100**, 231912, https://doi.org/10.1063/1.4724315 (2012).
40. Bouillard, J. S. G., Dickson, W., O'Connor, D. P., Wurtz, G. A. & Zayats, A. V. Low-temperature plasmonics of metallic nanostructures. *Nano Lett.* **12**, 1561–1565 (2012).
41. Alabastri, A., Toma, A., Malerba, M., De Angelis, F. & Zaccaria, R. P. High temperature nanoplasmonics: the key role of nonlinear effects. *ACS Photon.* **2**, 115–120 (2014).
42. Baffou, G. *et al*. Thermoplasmonics modeling: A Green"s function approach. *Phys. Rev. B* **82**, 165424, https://doi.org/10.1103/PhysRevB.82.165424 (2010).
43. Lang, S. *et al*. Dynamic measurement of near-field radiative heat transfer. *Sci. Rep.* **7**, 13916 (2017).
44. Tervo, E., Zhang, Z. & Cola, B. Collective near-field thermal emission from polaritonic nanoparticle arrays. *Phys. Rev. Mater.* **1**, 015201 (2017).
45. Biehs, S.-A., Rosa, F. S. S. & Ben-Abdallah, P. Modulation of near-field heat transfer between two gratings. *Appl. Phys. Lett.* **98**, 243102 (2011).
46. Candeo, A. & Dughiero, F. Numerical FEM models for the planning of magnetic induction hyperthermia treatments with nanoparticle. *IEEE Trans. Magn.* **45**, 1658–1661 (2009).
47. Yamada, I., Nishii, J. & Saito, M. Incident angle and temperature dependence of WSi wire-grid polarizer. *Infrared Phys. Technol.* **63**, 92–96 (2014).
48. Ma, K., Kim, D. J., Kim, K., Moon, S. & Kim, D. Target-localized nanograting-based surface plasmon resonance detection toward label-free molecular biosensing. *IEEE J. Sel. Top. Quantum Electron.* **16**(4), 1004–1014 (2010).
49. Moon, S. *et al*. Grating-based surface plasmon resonance detection of core-shell nanoparticle mediated DNA hybridization. *Biosens. Bioelectron.* **32**(1), 141–147 (2012).
50. Kim, Y., Chung, K., Lee, W., Kim, D. H. & Kim, D. Nanogap-based dielectric-specific colocalization for highly sensitive surface plasmon resonance detection of biotin-streptavidin interactions. *Appl. Phys. Lett.* **101**(23), 233701 (2012).
51. Oh, Y., Lee, W., Kim, Y. & Kim, D. Self-aligned colocalization of 3D plasmonic nanogap arrays for ultra-sensitive surface plasmon resonance detection. *Biosens. Bioelectron.* **51**, 401–407 (2014).
52. Cengel, Y. A. *Heat transfer: a practical approach* (2nd ed., McGraw Hill, 2003) Ch. 1, p. 25–27.
53. Baffou, G., Quidant, R. & García de Abajo, F. J. Nanoscale control of optical heating in complex plasmonic systems. *ACS Nano* **4**(2), 709–716 (2010).
54. Chen, X., Chen, Y., Yan, M. & Qiu, M. Nanosecond photothermal effects in plasmonic nanostructures. *ACS Nano* **6**, 2550–2557 (2012).
55. Baffou, G. *et al*. Photoinduced heating of nanoparticle arrays. *ACS Nano* **7**, 6478–6488 (2013).
56. Yi, F., Zhu, H., Reed, J. C., Zhu, A. Y. & Cubukcu, E. Thermoplasmonic membrane-based infrared detector. *IEEE Photon. Technol. Lett.* **26**, 202–205 (2014).
57. Johnson, P. B. & Christy, R. W. Optical constants of the noble metals. *Phys. Rev. B* **6**, 4370–4379 (1972).
58. Zhou, J. & Guo, L. J. Transition from a spectrum filter to a polarizer in a metallic nano-slit array. *Scientific Reports* **4**, 3614 (2014).
59. Wang, Z. *et al*. Plasmon–polaron coupling in conjugated polymer on infrared nanoantennas. *Nano Lett.* **15**, 5382–5387 (2015).
60. Lereu, A. L., Passian, A., Goudonnet, J. P., Thundat, T. & Ferrell, T. L. Optical modulation processes in thin films based on thermal effects of surface plasmons. *Appl. Phys. Lett.* **86**(15), 154101 (2005).
61. Boriskina, S. V. *et al*. Enhancement and tunability of near-field radiative heat transfer mediated by surface plasmon polaritons in thin plasmonic films. *Photonics* **2**, 659–683 (2015).
62. Wen, S.-B. Direct numerical simulation of near field thermal radiation based on Wiener chaos expansion of thermal fluctuating current. *J. Heat Transfer* **132**(7), 072704 (2010).
63. Guérout, R. *et al*. Enhanced radiative heat transfer between nanostructured gold plates. *J. Phys. Conf. Ser.* **395**, 012154, https://doi.org/10.1088/1742-6596/395/1/012154 (2012).
64. Russell, A. G., McKnight, M. D., Sharp, A. C., Hestekin, J. A. & Roper, D. K. Gold nanoparticles allow optoplasmonic evaporation from open silica cells with a logarithmic approach to steady-state thermal profiles. *J. Phys. Chem. C* **114**, 10132–10139 (2010).
65. Triambulo, R. E. & Park, J. W. Heat evolution and dissipation in organic light-emitting diodes on flexible polymer substrates. *Org. Electron.* **28**, 123–134 (2016).
66. Harris, N., Ford, M. J. & Cortie, M. B. Optimization of plasmonic heating by gold nanospheres and nanoshells. *J. Phys. Chem. B* **110**, 10701–10707 (2006).
67. Cao, L., Barsic, D. N., Guichard, A. R. & Brongersma, M. L. Plasmon-assisted local temperature control to pattern individual semiconductor nanowires and carbon nanotubes. *Nano Lett.* **7**, 3523–3527 (2007).
68. Fang, C., Shao, L., Zhao, Y., Wang, J. & Wu, H. A gold nanocrystal/poly (dimethylsiloxane) composite for plasmonic heating on microfluidic chips. *Adv. Mater.* **24**, 94–98 (2012).
69. Ramires, M. L. V. *et al*. Standard reference data for the thermal conductivity of water. *J. Phys. Chem. Ref. Data* **24**, 1377–1381 (1995).
70. Kadoya, K., Matsunaga, N. & Nagashima, A. Viscosity and thermal conductivity of dry air in the gaseous phase. *J. Phys. Chem. Ref. Data* **14**, 947–970 (1985).

Acknowledgements

This work was supported by the National Research Foundation (NRF) grants funded by the Korean Government (2015R1A2A1A10052826 and 2018R1D1A1B07042236). ES acknowledges the support by the grant from the National Research Foundation (2017R1A2B2003552).

Author Contributions

S.I. performed calculation, analyzed the data, and wrote the manuscript. E.S. wrote the manuscript. D.K. proposed the work and wrote the manuscript. Authors declare no competing interests. All the data are available upon request.

Additional Information

Competing Interests: The authors declare no competing interests.

Publisher's note: Springer Nature remains neutral with regard to jurisdictional claims in published maps and institutional affiliations.